Enhanced Energy Storage with Polar Vortices in Ferroelectric Nanocomposites

Zhen Liu, Bin Yang, Wenwu Cao, Edwin Fohtung, and Turab Lookman

Phys. Rev. Applied **8**, 034014 — Published 19 September 2017

DOI: 10.1103/PhysRevApplied.8.034014

Enhanced Energy Storage with Polar Vortices in Nanocomposites

Zhen Liu[1,2], Bin Yang[1], Wenwu Cao[1,3*], Edwin Fohtung[4], and Turab Lookman[2*]
[1] *Condensed Matter Science and Technology Institute and Department of Physics, School of Science, Harbin Institute of Technology, Harbin 150080, China*
[2] *Theoretical Division, Los Alamos National Laboratory, Los Alamos, New Mexico 87545, USA*
[3] *Materials Research Institute and Department of Mathematics, The Pennsylvania State University, University Park, Pennsylvania 16802, USA and*
[4] *Experimental Physics Division, Los Alamos National Laboratory, Los Alamos, New Mexico 87545, USA*
(Dated: August 22, 2017)

Nanocomposites of ferroelectric ceramic filler and polymer matrix show considerable promise as high energy storage dielectric capacitors. However, the influence of microstructure of the ferroelectric filler on the electric energy storage performance in the nanocomposite has not been quantitatively studied, yet it is a key element in understanding the methods employed to improve the performance of capacitors. We demonstrate an innovative strategy to enhance the energy storage density with topological vortex structures in nanocomposites. Using three dimensional phase field calculations, we show that multi-vortex structures can exist in ferroelectric nanowires without charge defects or free charges at the interface between the filler and matrix. The switching behavior of the topological structure (vortex and anti-vortex pair) under external electric field is calculated in nanocylinder wires. The small remnant polarization and very narrow hysteresis loop due to the vortex structure in the nanocomposites can lead to a large enhancement of energy density, as high as 5 J/cm^3 compared to 1-2 J/cm^3 for commercial capacitors, and high energy storage efficiency (over 95%) at a relatively low electric field of 140 MV/m.

PACS numbers: 77.80.bj, 77.80.Dj, 77.84.Lf

I. INTRODUCTION

Due to the increasing demand for advanced electronic devices and electric power systems with reduced weight, size and cost, the development of high power and high energy density dielectric materials is important. The energy density of commercial dielectric capacitors is usually of the order of 1-2 J/cm^3, far inferior to electrochemical capacitors ($\approx$ 20 J/cm^3) [1]. The energy density of a dielectric material is essentially given by U=$\int EdP$, where E is the electric field and P is the polarization. Therefore, materials with large polarization value and high electric breakdown field can potentially achieve a high energy density. Unfortunately, the currently available $BaTiO_3$ and PZT ferroelectric ceramics have relatively low breakdown strength. Although these materials have large polarization, the large remnant polarization (P_r) does not lead to high energy density due to the small field induced changes in polarization (shaded areas in Figure 1(a)). In high-quality ferroelectric/antiferroelectric thin films the energy storage density is much higher than that of ceramics due to the enhanced dielectric breakdown strength. For example, a very high energy storage density of 154 J/cm^3 at 218MV/m was achieved in the antiferroelectric film $(Bi_{1/2}Na_{1/2})_{0.9118}La_{0.02}Ba_{0.0582}(Ti_{0.97}Zr_{0.03})O_3$ [2], and recently Bin Xu *et al*[3] predicted via first principle calculations an energy storage density of 100-150 J/cm^3 in the lead free $Bi_{1-x}R_xFeO_3$ system. However, from a practical point of view, the energy density is determined by the processing method and quality of the film as failure is often driven by flaws. The current trend in searching for high energy density capacitors is to use polymer-matrix composites with ferroelectric fillers, combining high dielectric permittivity of the ceramic with high breakdown strength of the polymer [4–7]. Nanowires of $Ba_{0.2}Sr_{0.8}O_3$ nanocomposites have been reported to have an energy storage density as high as 14.86 J/cm^3 at 450 MV/m [8]. However, such large electric field strengths present a challenge to the supporting insulation systems in electronic devices, thus limiting the applications of miniaturized devices with a high level of integration. Moreover, the remnant polarization is still a negative factor for the high energy density in the polymer nanocomposites. Therefore, it is meaningful to develop large energy storage devices with comparable low electric field strengths. The energy utilization efficiency is another important factor for energy storage materials and is influenced by the closed area of the hysteresis loop [9, 10]. As shown in Figure 1(b), the charged energy density (J_c) is equal to the integral area enclosed by the charge curve and the y-axis, whereas the discharged energy density (J_d) is calculated by integrating the area enclosed by the discharge curve and the y-axis. The energy storage efficiency is J_d/J_c. Thus, a narrow hysteresis loop contributes to higher energy storage efficiency. The microstructure of the ferroelectric filler plays an important role in the dielectric property and electric energy density, but its influence on enhancing electric energy storage has been little studied and forms the focus of this work. The shape of fillers, charge defects and the inner stresses can affect the microstructure of the ferroelectric nanocomposite, thus impacting the electric energy storage and ultimately the design and optimization. We focus here on exploring the effects of polarization vortices on properties of ferroelectric composites.

The vortex domain structure has been observed in ferroelectric nanoparticles[11, 12]. And polar vortices in superlattices demonstrated in Ref.[13] have been directly observed recently in $PbTiO_3/SrTiO_3$ superlattices[14], although non uniform domain morphologies were first studied using an electrostatic model in Ref.[15]. The vortex-to-polarization phase transition in $Pb(ZrTi)O_3$ nanoparticles[16] was first predicted on the basis of ab-initio calculations. Thereafter, vortex states with geometrical textures and critical temperatures were studied in two dimensional systems[17]. In ferroelectric nanowires (NWs), the vortex structure has also been inferred via first-principle calculations[18]. A novel vortex core transition and phase-locking of ferroelectric vortices accompanied by the formation of antivortices was predicted in $BaTiO_3/SrTiO_3$ nanocomposites[19] using first principles calculations. A three dimensional phase field study of domain structure in ferroelectric nanorods of different shapes and sizes was carried out by Slutsker *et al.* The possible applications of topological defects in electronic devices were investigated in the past decade[20–22]. Experimentally, electric conductivity was explored to be enhanced at the vortex cores in $BiFeO_3$[20], which is related to a form of modified band alignment as predicted by *ab inito* calculations[22]. Topologically, the ferroelectric vortex phase is expected to increase the information storage density by 5 orders of magnitude in memory devices[21]. The application of ferroelectric vortex in electric energy storage has not been previously considered. In this work, we show that in nanocomposites with $BaTiO_3$ embedded in a non-ferroelectric polymer matrix, a topological vortex and anti-vortex phase can coexist if no free charges are present at the interface between the filler NWs and the matrix. This vortex structure undergoes a very different phase transition from that observed in common nonlinear dielectric materials. It leads to an almost zero remnant polarization P_r and a very narrow P-E hysteresis loop, resulting in a large energy storage density and efficiency even at relatively low electric fields. This finding provides us with a new approach to enhance the electric energy storage of dielectric capacitors.

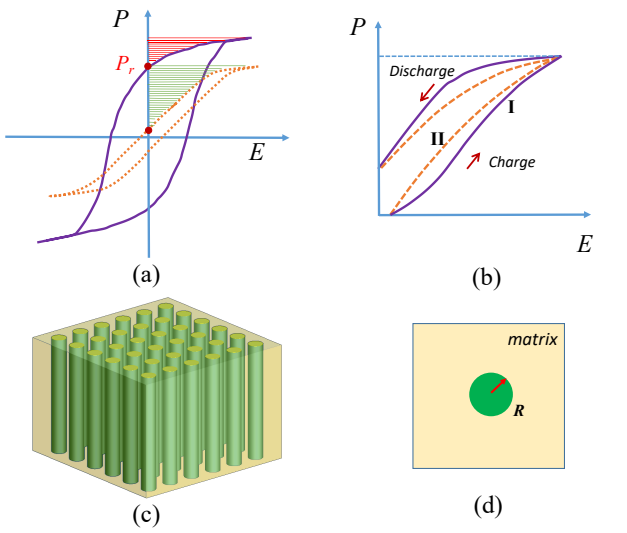

FIG. 1. (a) Schematic illustration of P-E hysteresis loops for the energy storage of ferroelectric materials with small remnant polarization P_r. The shaded green and red areas of the hysteresis loops indicate the available energy density. (b) Schematic illustration of the effect of the closed area of the hysteresis loops on energy storage efficiency, the narrow P-E loop II compared to loop I has a larger energy storage density and efficiency. (c) Schematic diagram of nanowire arrays embedded in non-ferroelectric matrix. (d) Schematic diagram of the model of the nanowire with a radius R in the matrix in the simulation.

II. THEORETICAL MODEL

The microstructure and dielectric property of nanocomposites can be calculated by employing phase field simulations based on mesoscale Landau theory in which the phase structure is described by the distribution of polarization $\mathbf{P}(\mathbf{r})$. To model the ferroelectric nanowire (NW) arrays embedded in the non-ferroelectric polymer matrix as shown in Figure 1(c), we have simulated the evolution of the polarization in the NWs, while maintaining a fixed polarization $\mathbf{P} \approx \varepsilon_m\varepsilon_0\mathbf{E}$ for different external electric fields $\mathbf{E}$ in the matrix, where ε_0 is the vacuum dielectric permittivity, and ε_m denotes the permittivity of the matrix material. We assume that the system is free of charge defects and no space charges exist at the interface between the ferroelectric filler and the dielectric matrix. The equilibrium state is described by the polarization distribution corresponding to the minimum free energy state. The total free energy of the NWs can be written as[23]:

$$F = \int d^3r \left[f(\mathbf{P}) + \frac{1}{2}\beta_{ijkl}\nabla_i P_j \nabla_k P_l - \mathbf{E}\cdot\mathbf{P} \right] + \frac{1}{2}\int \frac{d^3k}{(2\pi)^3} \left[\frac{k_i k_j}{\varepsilon_0\varepsilon_b k^2}\widetilde{P}_i\widetilde{P}_j^* + K_{ijkl}\widetilde{\varepsilon}_{ij}^0\widetilde{\varepsilon}_{kl}^{0*} \right] \quad (1)$$

where

$$\begin{aligned} f(\mathbf{P}) =& \alpha_1(P_1^2+P_2^2+P_3^2) + \alpha_{11}(P_1^4+P_2^4+P_3^4) \\ &+ \alpha_{12}(P_1^2P_2^2+P_2^2P_3^2+P_3^2P_1^2) \\ &+ \alpha_{111}(P_1^6+P_2^6+P_3^6) + \alpha_{112}[P_1^4(P_2^2+P_3^2) \\ &+ P_2^4(P_1^2+P_3^2) + P_3^4(P_1^2+P_2^2)] \\ &+ \alpha_{123}P_1^2P_2^2P_3^2 \end{aligned} \quad (2)$$

is the Landau-Devonshire free energy density, and $\alpha_1, \alpha_{11}, \alpha_{111}, \alpha_{12}, \alpha_{112}, \alpha_{123}$ are the Landau coefficients. The gradient term in Eq.(1) denotes the energy contribution from the polarization changes in the NW and interfaces, $\nabla_i = \partial/\partial_i$ is the gradient operator and β_{ijkl} is the gradient coefficient. The $\mathbf{k}$ space integral in Eq.(1) represents the electrostatic energy and the elastostatic energy, in which ε_0 and ε_b are the permittiv-

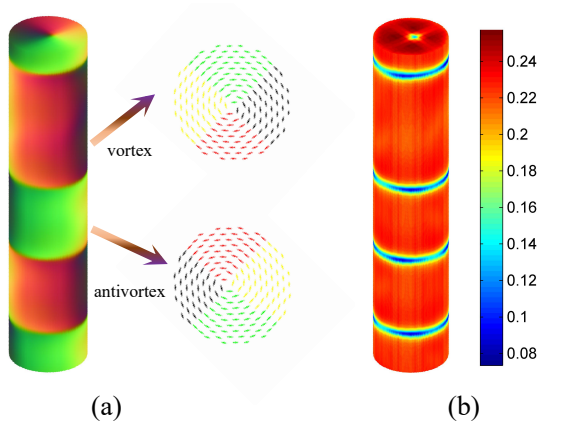

FIG. 2. Topological domain structures in the nanowire. (a) The domain structure of the NW is visualized by color maps in red, green, and blue (RGB) for components P_x, P_y, and P_z, the colored arrows denote the in-plane polarization directions P_x, P_y; vortex and antivortex domains coexist in the nanowire. (b) The distribution of the magnitude of polarization in the nanowire.

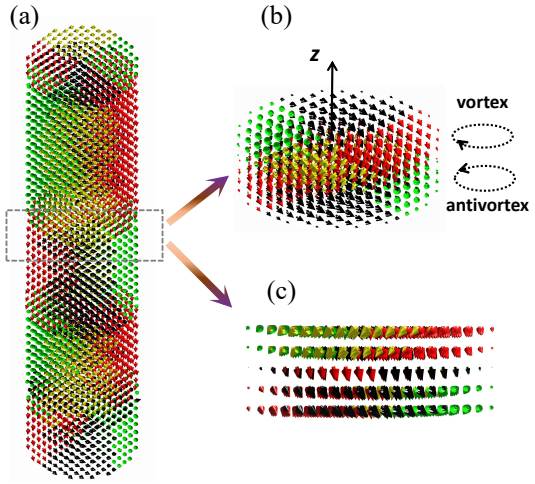

FIG. 3. (a) Polarization distribution in the $R = 22.4$ nm NW. (b)(c) The polarization changes across the domain wall.

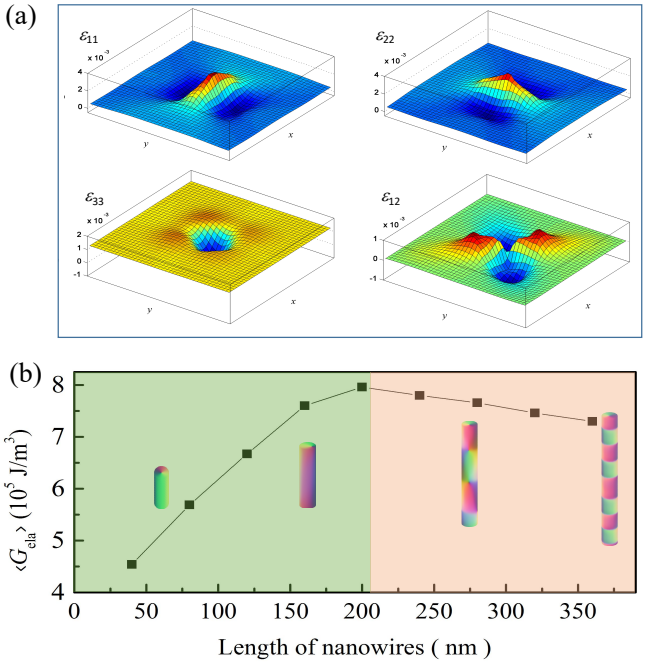

FIG. 4. (a) The distribution of the total strain $\varepsilon_{11}, \varepsilon_{22}, \varepsilon_{33}$, and ε_{12} in the top plane of the NW. (b) The average total elastic energy density $\langle G_{ela} \rangle$ with the length of the NWs. $\langle G_{ela} \rangle$ increases with the length of the NW, multi-vortex structure exists in order to decrease the elastic energy.

ity of vacuum and background permittivity of the material, respectively. $K_{ijkl} = C_{ijkl} - n_m C_{ijmn} \Omega_{np} C_{klpq} n_q$, $\Omega_{ik} = (C_{ijkl} n_j n_l)^{-1}$, C_{ijkl} is the elastic stiffness constant tensor and $\mathbf{n} = \mathbf{k}/k$ is the unit wave vector. The spontaneous strain ε^0_{ij} is given by $\varepsilon^0_{ij} = Q_{ijkl} P_k P_l$, where Q_{ijkl} is the electrostrictive coefficient. The elastic moduli are assumed to be equal in the nanowires and matrix. In Eq.(1), $\widetilde{P}_i$ and $\widetilde{\varepsilon}^0_{ij}$ are the Fourier transforms of P_i and ε^0_{ij}. The temporal evolution of the polarization can be obtained by solving the time-dependent Ginzburg-Landau equation[24]:

$$\frac{\delta P_i(\mathbf{r}, t)}{\delta t} = -L \frac{\delta F}{\delta P_i(\mathbf{r}, t)}, (i = 1, 2, 3) \qquad (3)$$

where L is the kinetic coefficient. In our phase field simulation, a $40 \times 40 \times 128$ grid with 4.24 nm spatial steps is used to simulate the NW embedded in a dielectric matrix. The core part is the infinite cylindrical NW with a radius R while the outer part is the non-ferroelectric medium in Figure 1(d). Periodic boundary conditions are used in all three axial directions to model the infinite NW arrays in the matrix. The Landau parameters are taken from Ref.[25]. The elastic constants $C_{11} = 17.8 \times 10^{10}$ N/m^2, $C_{12} = 9.6 \times 10^{10}$ N/m^2, and $C_{44} = 12.2 \times 10^{10}$ N/m^2, the electrostrictive constants are $Q_{11} = 0.11$ m^4/C^2, $Q_{12} = -0.034$ m^4/C^2, and $Q_{44} = 0.059$ m^4/C^2, the background permittivity ε_b is set as 100 in ferroelectric NWs and $\varepsilon_m = 3$ in dielectric matrix.

III. RESULTS AND DISCUSSIONS

The mechanism for the formation of vortex domains is the competition between the elastic energy, the electrostatic energy and the gradient energy. The elastic energy, which arises from the fact that $BaTiO_3$ NWs are constrained by the non-ferroelectric polymer matrix, drives the NWs to adopt a mixture of in-plane P_x, P_y and out-of-plane P_z polarizations. The second major contribution is the electrostatic energy induced by the built-in electric fields. If the interface between the ferroelectric NWs and the non-ferroelectric matrix is charge free or has a very small charge density, i.e., $\nabla \cdot \mathbf{P} \approx 0$, the polarizations

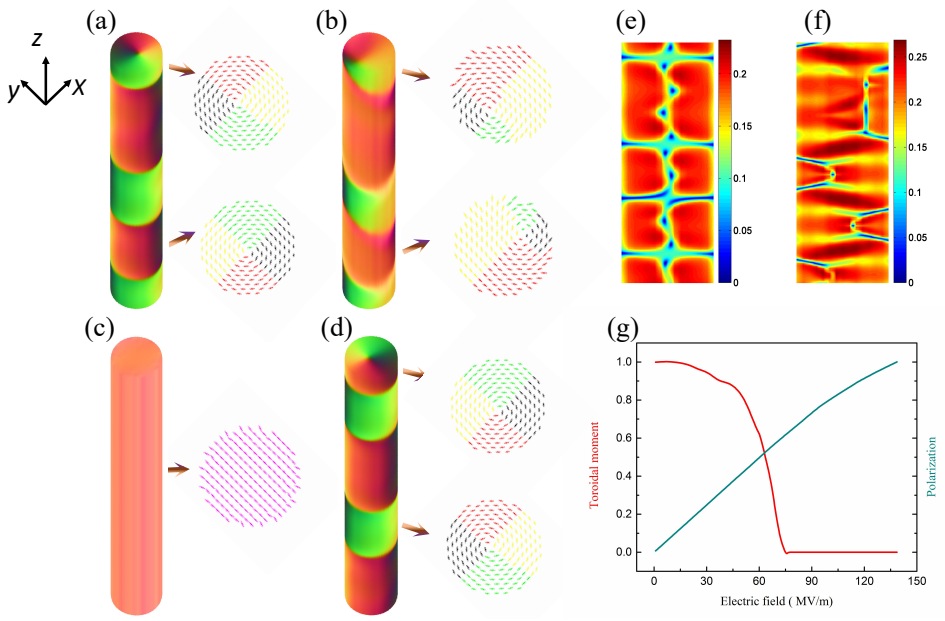

FIG. 5. The dynamic behavior of the vortex structure under an external electric field along [010] direction. (a)(b)(c)(d) show the domain switching with increasing electric field. (a) $E = 0$, the vortex core is along the axis of the NWs, (b) $E = 55.4$ MV/m, the vortex and anti-vortex display reverse switching behavior, the cores of the vortex and antivortex move to the edge of the NWs but in opposite direction along the x-axis. (c) $E = 110.9$ MV/m, the domains are poled to a single domain along [010] and the topological structures disappear. (d) The vortex structure appears again with the electric field decreasing to zero. (e)(f) show the topological core lines of vortex structure across the inner length-wise cross section of the nanowire at E=0 and E=55.4MV/m, respectively. (g) The average polarization along the field direction and the behavior of the toroidal moment vs. the field.

tend to align parallel to the interface. Finally, the gradient energy tends to change the direction and magnitude of the polarization. The three energy contributions lead to the topological structure in the NWs. The domain structure of the NW is visualized by color maps in red, green, and blue (RGB) for components P_x, P_y, and P_z, respectively, as shown in Figure 2(a) (Ploting details are given in the Supplemental Material[26]), and the colored arrows represent the in-plane polarization distribution P_x, P_y corresponding to the vortex structures in Figure 2(a). Unlike the reported multi-vortex structures in nano-geometries confined in a two dimensional plane[17], the vortex (in the clockwise direction) and antivortex (counter clockwise direction) structures coexist along the axis of the $R = 22.4$ nm NW in the absence of an external electric field, but not in the same plane. Figure 2(b) shows the magnitude of the polarization in the NW. The blue color in the center of the NW represents the vortex core and the blue bands on the wire indicate the domain walls that separate the vortex and anti-vortex domains. The spontaneous polarization of the vortex domain in the ferroelectric NWs is about 0.24 C/m^2. The exact distribution of the polar vector $P(P_x, P_y, P_z)$ is shown in Figure 3(a), the in-plane polarization P_x, P_y form the vortex-antivortex structures, while there is a polarization component, P_z, out of plane along the z-axis. Figures 3(b)(c) show clearly that the polarization changes across the vortex-antivortex domain wall shown by the dashed rectangular region in Figure 3(a). The arrows at the domain wall denote the small magnitude of polarization corresponding to Figure 2(b).

Figure 4(a) shows the components of the total elastic strain tensor, that is, ε_{11}, ε_{22}, ε_{33}, and ε_{12} in the top plane of the NW. The patterns of the strain components are similar to that of first principle calculations in PZT nanodots[27] with large values of ε_{11}, ε_{22} near the vortex core. However, the magnitude of the strains are smaller in the NW case due to the constraint of the matrix and smaller spontaneous polarization of $BaTiO_3$. The symmetry of the ε_{12} strain pattern together with ε_{11}, ε_{22} can guide experiments towards finding topological vortices in ferroelectric nanowires. The reason for the existence of the vortex-anti-vortex pair is due to the competition between the gradient energy and elastic energy. The multi-vortex structure will increase the gradient energy due to changes in polarization across the domain wall, but will decrease the total elastic energy. For R=22.4 nm NWs with short length, a single vortex exists as the gradient energy is the principal contributor. The average elastic energy density $\langle G_{ela} \rangle$ is obtained from $\langle G_{ela} \rangle = \frac{F_{ela}}{V}$, where F_{ela} is the total elastic energy and V is the volume of the NW. The energy $\langle G_{ela} \rangle$ increases with length below 200 nm, as shown in Figure 4(b). Above 200 nm, if no transition from single vortex to multivortex in the nanowire occurs, then $\langle G_{ela} \rangle$ would continue to increase. Thus, the elastic energy is a major contributor in the

transition from single vortex to multivortex structures in order to decrease the elastic energy (See Figure S4 in Supplemental Material[26]). The decreasing of $\langle G_{ela} \rangle$ in Figure 4(b) above 200 nm is accompanied by an increase in the number of vortex-antivortex pairs.

In order to investigate the dielectric response, we applied an external electric field along the y-axis to study the dynamic properties of the vortex domains in the NWs. This is shown in Figure 5 for the NW with R=22.4 nm. The vortex center is along the axis of the NW at zero applied electric field in Figure 5(a). With increasing electric field, the vortex and anti-vortex display reverse switching behavior: the anti-vortex center moves towards the negative x direction whereas the vortex moves towards the opposite direction as shown in Figure 5(b). When the electric field is large enough at 110.9 MV/m, both the vortex and anti-vortex structures switch to a single domain phase with polarization along [010] direction as shown in Figure 5(c). In order to show the vortex movement inside the NWs, the magnitude of the polarization distribution in the $y = 0$ plane was calculated. In Figure 5(e) the vortex core (blue color) acts as a line defect, usually regarded as an Ising line [28], in the center of the NW at zero field. At a field value of $E = 55.4$ MV/m, as shown in Figure 5(f), the Ising line passing through the vortex and anti-vortex cores separates into two parts, one associated with the vortices and the other with the anti-vortices. However, when the field decreases to zero, the vortex and anti-vortex structures reappear as show in Figure 5(d), and the average polarization along the field direction [010] is zero in the vortex. Thus, macroscopically this corresponds to a zero remnant polarization of the nanocomposite capacitor. Figure 5(g) depicts the normalized average polarization along [010] and the toroidal moment $TM = \frac{1}{TM_0} \int \mathbf{r} \times \mathbf{P}$ as a function of the electric field, where TM_0 denotes the value of the toroidal moment without field. The polarization along [010] increases with the electric field, whereas the toroidal moment decreases with the field. At $E = 75$ MV/m, the zero value of TM indicates a special vortex-to-polarization phase transformation in the ferroelectric NW.

Since the vortex structure is sensitive to the size of the NW, we carried out several simulations with increasing NW radius R. If $R = 57$ nm, the resulting domain structure is no longer regular as previously described. The structures for the NW are now far more complex as shown in Figure 6(a)(b), where the blue arrows denote the in plane polarization at the top face of the NW. A vortex - anti-vortex pair can now coexist in one plane.

The electrical hysteresis loops for different NW R values are calculated in Figure 7. As R increases from 32 nm to 57 nm, the saturation polarization increases from 3 μC/cm^2 to about 10 μC/cm^2. Compared to the hysteresis loop for bulk $BaTiO_3$ [29], our NW $BaTiO_3$ nanocomposites have an almost zero remnant polarization due to the vortex structure, and very slimmer hysteresis loops. Thus, the almost zero remnant polarization

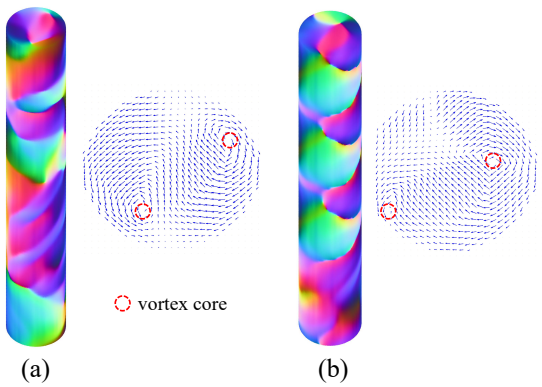

FIG. 6. Domain distribution of NWs with a radius of 57 nm, two vortices exist on certain cross-sections of the NW, the arrows show the polarization distribution on the top plane. (a) The unpoled domain structure. (b) The poled domain structure.

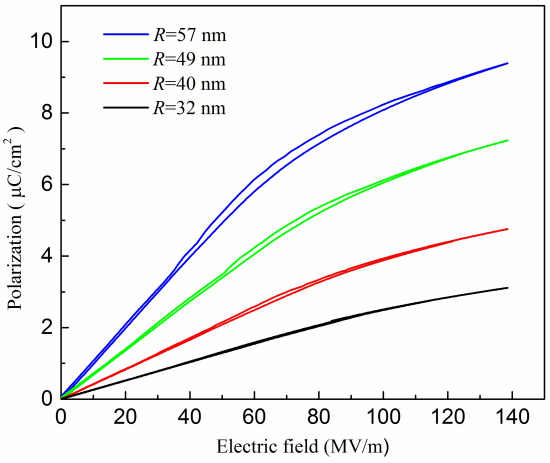

FIG. 7. The calculated P-E loop with increasing the radius R of the NWs.

and very small closed area of the P-E loops associated with the topological structures lead to considerable enhancement of the energy density in our NW composites. The exact energy storage densities as a function of increasing R from 32 nm to 57 nm are shown in Figure 8(a). The energy density increases from 1.8 J/cm^3 to 5.0 J/cm^3 at 140 MV/m as R increases. The reported energy density for the nanocomposites with $BaTiO_3$ nanoparticles embedded in TiO_2 nanofibers in poly(vinylidene fluoride) matrix (PVDF/BTO@TO_nfs) is about 1.4 J/cm^3 and 1.7 J/cm^3 for the 7.5% $Ba_{0.2}Sr_{0.8}TiO_3$ NWs in poly(vinylidene fluoride) nanocomposites at the same field[1, 8, 30](See Figure 8(a)). The enhancement of the energy density is about 3 fold due to the polar vortex structures. Figure 8(b) shows the caluculated energy storage efficiency with the increasing of the radius R, the energy efficiency decreases. However, the efficiency is over 95% at $R = 57$ nm, which is higher than that of

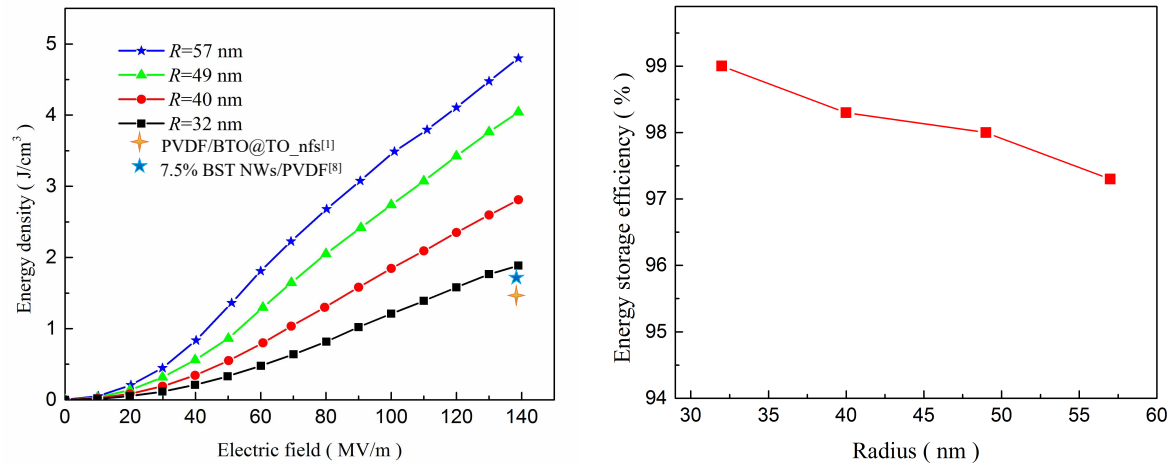

(a) (b)

FIG. 8. (a) The calculated energy storage density with increasing the radius R of the NWs. At a relatively low electric field of about 140 MV/m, the energy density can reach as high as 5 J/cm^3 compared to 1.5 J/cm^3 of recently reported nanocomposite materials. (b) The calculated energy storage efficiency vs. the radius R

the reported $BaTiO_3$@$SrTiO_3$ ceramics (about 90%)[9].

IV. CONCLUSIONS

In conclusion, we have studied the dielectric properties of cylindrical nanowire composites consisting of ferroelectric filler in a polymer matrix with coexisting vortex and anti-vortex structures using phase field simulations. The special vortex-to-polarization phase transformation under an electric field leads to an almost zero remnant polarization and a very slim hysteresis loop, which significantly enhances the energy density and efficiency in the nanocomposites. Even at a relatively low electric field of 140 MV/m, the energy density can reach as high as 5 J/cm^3 compared to 1.5 J/cm^3 of recently reported nanocomposite materials, and the energy efficiency is above 95%. Our results suggest an alternate strategy to improve the electrical energy storage in composite dielectric capacitors. Experimentally, oxygen vacancies or other charge defects in the ferroelectric NWs can potentially affect the the formation of topological vortex structures. Hence, our work should motivate experiments to further decrease concentrations of defects and free charges at interfaces between ferroelectric fillers and matrices to produce dielectric capacitors with enhanced energy storage capacity.

ACKNOWLEDGMENTS

The work was supported by the National Key Basic Research Program of China (Grant No.2013CB632900), the State Scholarship Fund of the China Scholarship Council (No.201506120195) and by Los Alamos National Laboratory.

[1] Xin Zhang, Yang Shen, Qinghua Zhang, Lin Gu, Yuhan Hu, Jiawen Du, Yuanhua Lin, and Ce-Wen Nan, "Ultrahigh energy density of polymer nanocomposites containing $BaTiO_3$@TiO_2 nanofibers by atomic-scale interface engineering," Advanced Materials **27**, 819–824 (2015).

[2] Biaolin Peng, Qi Zhang, Xing Li, Tieyu Sun, Huiqing Fan, Shanming Ke, Mao Ye, Yu Wang, Wei Lu, Hanben Niu, James F. Scott, Xierong Zeng, and Haitao Huang, "Giant electric energy density in epitaxial lead-free thin films with coexistence of ferroelectrics and antiferroelectrics," Advanced Electronic Materials **1** (2015).

[3] Bin Xu, Jorge Íñiguez, and L Bellaiche, "Designing lead-free antiferroelectrics for energy storage," Nature Communications **8** (2017).

[4] Junjun Li, Jason Claude, Luis Enrique Norena-Franco, Sang Il Seok, and Qing Wang, "Electrical energy storage in ferroelectric polymer nanocomposites containing surface-functionalized $BaTiO_3$ nanoparticles," Chemistry of Materials **20**, 6304–6306 (2008).

[5] Junjun Li, Sang Il Seok, Baojin Chu, Fatih Dogan, Qiming Zhang, and Qing Wang, "Nanocomposites of ferroelectric polymers with TiO_2 nanoparticles exhibiting significantly enhanced electrical energy density," Advanced Materials **21**, 217–221 (2009).

[6] Xingyi Huang and Pingkai Jiang, "Core–shell structured high-k polymer nanocomposites for energy storage and dielectric applications," Advanced Materials **27**, 546–554 (2015).

[7] Ke Yang, Xingyi Huang, Yanhui Huang, Liyuan Xie, and Pingkai Jiang, "Fluoro-polymer@$BaTiO_3$ hybrid nanoparticles prepared via RAFT polymerization: toward ferroelectric polymer nanocomposites with high dielectric constant and low dielectric loss for energy storage application," Chemistry of Materials **25**, 2327–2338 (2013).

[8] Haixiong Tang and Henry A Sodano, "Ultra high energy density nanocomposite capacitors with fast discharge using $Ba_{0.2}Sr_{0.8}TiO_3$ nanowires," Nano letters **13**, 1373–1379 (2013).

[9] Longwen Wu, Xiaohui Wang, Huiling Gong, Yanan Hao, Zhengbo Shen, and Longtu Li, "Core-satellite $BaTiO_3$@$SrTiO_3$ assemblies for a local compositionally graded relaxor ferroelectric capacitor with enhanced energy storage density and high energy efficiency," Journal of Materials Chemistry C **3**, 750–758 (2015).

[10] Sheng Tong, Beihai Ma, Manoj Narayanan, Shanshan Liu, Rachel Koritala, Uthamalingam Balachandran, and Donglu Shi, "Lead lanthanum zirconate titanate ceramic thin films for energy storage," ACS applied materials & interfaces **5**, 1474–1480 (2013).

[11] Alexei Gruverman, D Wu, HJ Fan, I Vrejoiu, M Alexe, RJ Harrison, and JF Scott, "Vortex ferroelectric domains," Journal of Physics: Condensed Matter **20**, 342201 (2008).

[12] BJ Rodriguez, XS Gao, LF Liu, W Lee, II Naumov, AM Bratkovsky, D Hesse, and M Alexe, "Vortex polarization states in nanoscale ferroelectric arrays," Nano letters **9**, 1127–1131 (2009).

[13] Pavlo Zubko, N Jecklin, Almudena Torres-Pardo, P Aguado-Puente, A Gloter, Céline Lichtensteiger, J Junquera, O Stéphan, and J-M Triscone, "Electrostatic coupling and local structural distortions at interfaces in ferroelectric/paraelectric superlattices," Nano letters **12**, 2846–2851 (2012).

[14] AK Yadav, CT Nelson, SL Hsu, Z Hong, JD Clarkson, CM Schlepütz, AR Damodaran, P Shafer, E Arenholz, LR Dedon, D Chen, A Vishwanath, AM Minor, LQ Chen, JF Scott, Martin. LW, and R Ramesh, "Observation of polar vortices in oxide superlattices," Nature **530**, 198–201 (2016).

[15] F De Guerville, I Lukyanchuk, L Lahoche, and M El Marssi, "Modeling of ferroelectric domains in thin films and superlattices," Materials Science and Engineering: B **120**, 16–20 (2005).

[16] Ivan Naumov and Huaxiang Fu, "Vortex-to-polarization phase transformation path in ferroelectric $Pb(ZrTi)O_3$ nanoparticles," Physical review letters **98**, 077603 (2007).

[17] L Lahoche, I Luk'Yanchuk, and G Pascoli, "Stability of vortex phases in ferroelectric easy-plane nano-cylinders," Integrated Ferroelectrics **99**, 60–66 (2008).

[18] G Pilania and R Ramprasad, "Complex polarization ordering in $PbTiO_3$ nanowires: A first-principles computational study," Physical Review B **82**, 155442 (2010).

[19] Lydie Louis, Igor Kornev, Grégory Geneste, Brahim Dkhil, and L Bellaiche, "Novel complex phenomena in ferroelectric nanocomposites," Journal of Physics: Condensed Matter **24**, 402201 (2012).

[20] Nina Balke, Benjamin Winchester, Wei Ren, Ying Hao Chu, Anna N Morozovska, Eugene A Eliseev, Mark Huijben, Rama K Vasudevan, Petro Maksymovych, Jason Britson, Stephen Jesse, Igor Kornev, Ramamoorthy Ramesh, Laurent Bellaiche, Long Qing Chen, and Sergei V.Kalinin, "Enhanced electric conductivity at ferroelectric vortex cores in $BiFeO_3$," Nature Physics **8**, 81 (2012).

[21] Ivan I Naumov, L Bellaiche, and Huaxiang Fu, "Unusual phase transitions in ferroelectric nanodisks and nanorods," Nature **432**, 737–740 (2004).

[22] Zhigang Gui, Lin-Wang Wang, and L Bellaiche, "Electronic properties of electrical vortices in ferroelectric nanocomposites from large-scale ab initio computations," Nano letters **15**, 3224–3229 (2015).

[23] Wei-Feng Rao and Yu U Wang, "Domain wall broadening mechanism for domain size effect of enhanced piezoelectricity in crystallographically engineered ferroelectric single crystals," Applied physics letters **90**, 041915 (2007).

[24] Zhen Liu, Bin Yang, Wenwu Cao, and Turab Lookman, "Effect of misfit strain on ferroelectric domain formation at the morphotropic phase boundary," Physical Review B **94**, 214117 (2016).

[25] Tomas Sluka, Alexander K Tagantsev, Dragan Damjanovic, Maxim Gureev, and Nava Setter, "Enhanced electromechanical response of ferroelectrics due to charged domain walls," Nature communications **3**, 748 (2012).

[26] See Supplemental Material at [URL will be inserted by publisher] for the plotting details of domain structures in the Nanowires.

[27] S Prosandeev and L Bellaiche, "Characteristics and signatures of dipole vortices in ferroelectric nanodots: First-principles-based simulations and analytical expressions," Physical Review B **75**, 094102 (2007).

[28] V Stepkova, P Marton, and J Hlinka, "Ising lines: Natural topological defects within ferroelectric bloch walls," Physical Review B **92**, 094106 (2015).

[29] H Basantakumar Sharma, HNK Sarma, and A Mansingh, "Ferroelectric and dielectric properties of sol-gel processed barium titanate ceramics and thin films," Journal of materials science **34**, 1385–1390 (1999).

[30] Penghao Hu, Yang Shen, Yuhan Guan, Xuehui Zhang, Yuanhua Lin, Qiming Zhang, and Ce-Wen Nan, "Topological-structure modulated polymer nanocomposites exhibiting highly enhanced dielectric strength and energy density," Advanced Functional Materials **24**, 3172–3178 (2014).